MNRAS 000, 1–18 (2026) Preprint 20 January 2026 Compiled using MNRAS LATEX style file v3.3

A novel method of point-spread function fitting to extract TESS light curves: ensemble analysis of massive star variability in the SMC

Pieterjan J. Van Daele,[1]★ Dominic M. Bowman,[1,2], J. Bodensteiner,[3], T. Shenar,[4]
[1]School of Mathematics, Statistics and Physics, Newcastle University, Newcastle upon Tyne, NE1 7RU, UK
[2]Institute of Astronomy, KU Leuven, Celestijnenlaan 200D, B-3001 Leuven, Belgium
[3]Anton Pannekoek Institute for Astronomy, University of Amsterdam, Science Park 904, 1098 XH Amsterdam, The Netherlands
[4]The School of Physics and Astronomy, Tel Aviv University, Tel Aviv 6997801, Israel

Accepted XXXX. Received YYYY; in original form ZZZZ

ABSTRACT

Massive stars, the progenitors of neutron stars and black holes, play a crucial role in shaping the chemical and radiative properties of entire galaxies through their winds and explosive deaths. The efficiency of pulsation excitation mechanisms is strongly dependent on a star's metallicity. However, this remains largely uncalibrated in evolution models, due to a lack of a sufficient sample of stars at different metallicities, with data suitable for asteroseismology — the study of stellar pulsations. Obtaining TESS light curves for low-metallicity stars beyond the Milky Way is challenging, due to the stars being faint and heavily crowded. In this paper, we present a novel PSF based light curve extraction method overcoming these challenges and demonstrate the limitations of the often-used simple aperture photometry (SAP) method that can provide heavily contaminated light curves. With this PSF technique, accurate light curves of 91 SMC massive stars are extracted. They reveal a variety of variability types including indications of binarity and stellar pulsations (e.g. coherent modes and stochastic low frequency variability). We also explore the SLF variability for massive stars in the Small Magellanic Cloud and demonstrate how its morphology probes a star's location in the Hertzsprung–Russell diagram and is similar to galactic massive stars, which indicates the underlying physical mechanism is insensitive to metallicity.

Key words: techniques: photometric - asteroseismology - stars: oscillations - stars: early-type - stars: evolution - stars: binarity

1 INTRODUCTION

Massive stars have birth masses above about 8 $M_\odot$ and are progenitors of supernovae events, which means they are also the precursors of neutron stars and black holes (Maeder & Meynet 2000; Kippenhahn et al. 2012; Langer 2012). Through their radiative winds and explosive deaths, massive stars are important chemical factories in the Universe, and play a major role in the study of star formation, galactic evolution (Hopkins et al. 2014), binary systems (Sana et al. 2012; Marchant & Bodensteiner 2024), and gravitational waves (Abbott et al. 2016).

Current stellar evolution models, however, contain large uncertainties in how these stars are born, evolve and die. Specifically, we lack accurate prescriptions of interior rotation, chemical mixing, and the transport of angular momentum (Aerts et al. 2019). Moreover, ongoing research has shown the importance of mixing and angular momentum transport by internal gravity waves (IGWs; Rogers & McElwaine 2017; Varghese et al. 2023, 2025), which is currently not fully implemented in 1D stellar evolution models. With larger internal mixing, unprocessed hydrogen is transported from the envelope into the core and made available for nuclear burning, which allows the star to spend longer on the hydrogen-burning main sequence, resulting in a larger helium core mass at the end of the main sequence (see Bowman 2020; Johnston 2021). In turn this affects the evolution beyond the main sequence and therefore also the supernovae chemical yields (Maeder & Meynet 2000; Kippenhahn et al. 2012; Langer 2012).

The ongoing advances in asteroseismology, the study of stellar pulsations (Aerts et al. 2010), enables us to empirically probe and constrain the physical mechanisms and processes inside stars (Aerts 2021). Historically, coherent heat-driven pulsations have been exploited for massive stars for several decades (see Bowman 2020 for a review), which are excited by an iron-opacity bump near the surface for masses above about 3 $M_\odot$ and ages that span the entire main-sequence and beyond (Dziembowski & Pamyatnykh 1993; Miglio et al. 2007; Burssens et al. 2020). More recently, damped pulsation modes (i.e. propagating waves rather than coherent standing waves) generated at the turbulent interface of convective and radiative regions have been detected for hundreds of massive stars in the Milky Way galaxy (Bowman et al. 2019a,b, 2020), but also for massive stars in the LMC and SMC galaxies (Bowman et al. 2019a, 2024). This new type of asteroseismic signal is referred to as stochastic low-frequency (SLF) variability, and has great potential for probing the interior physics of massive stars that lack coherent heat-driven pulsation modes (see Bowman 2023 for a review). This signal is thought to be caused by IGWs excited at the boundary of convective regions based on hydrodynamical simulations of stellar interiors (Rogers et al. 2013; Aerts & Rogers 2015; Rogers & McElwaine

★ E-mail: p.van-daele2@newcastle.ac.uk

2017; Edelmann et al. 2019; Schultz et al. 2022; Anders et al. 2023; Thompson et al. 2024).

Stars in the SMC have a much lower metallicity compared to galactic stars (i.e. $Z_{\rm SMC} \simeq 0.2\,Z_{\odot}$; Hunter et al. 2007). Therefore, the opacity in the sub-surface convection zones of massive stars is lower compared to galactic stars. This means that convection is less efficient and may carry only a small fraction of the flux, or sub-surface convection zones may even be absent entirely. For example, even for galactic massive stars, convection is only a minor contributor to the total flux and energy transport in these turbulent sub-surface regions (see e.g. Debnath et al. 2024). Since low-metallicity main-sequence massive stars may lack sub-surface convection zones entirely (Jermyn et al. 2022; Bowman et al. 2024), SLF variability in such stars would therefore originate from the only remaining convection zone: the convective core. Bowman et al. 2024 performed a proof-of-concept study of studying SLF variability in LMC and SMC massive stars and found little difference in the amplitudes or dominant frequency range of SLF variability compared to galactic massive stars. However, a systematic and detailed characterisation of SLF variability for SMC massive stars across the Hertzsprung–Russell (HR) diagram is yet to be performed. This is important to constrain, in particular because IGWs are efficient transporters of chemical species and angular momentum (Rogers & McElwaine 2017; Varghese et al. 2025). Hence, IGWs and SLF variability represent crucial pieces of the stellar evolution puzzle.

In addition to different types of stellar pulsations, variability in a light curve can also have other causes such as binarity or chemical spots on a rotating (chemically peculiar and/or magnetic) star, for which photometric light curves complement spectroscopic studies. In this paper we focus on massive stars from the BLOeM sample (Shenar et al. 2024; see also Section 2.1). BLOeM (Binarity at LOw Metallicity) is a survey that collects multi-epoch spectroscopy of almost 1000 SMC stars and studies various different aspects of physics of massive stars, with a strong focus on binarity and multiplicity. Recent work includes the estimation of the binary fraction of blue supergiants in the SMC (Britavskiy et al. 2025), the multiplicity properties of BAF-type supergiants (Patrick et al. 2025) and rapidly rotating Oe and Be stars (Bodensteiner et al. 2025). Furthermore, Sana et al. 2025 showed that a high proportion of O-type stars in the SMC have a close companion, which implies that binary interaction likely plays a dominant role in shaping massive-star evolution in metal-poor, early-Universe environments. Obtaining light curves for BLOeM targets is therefore not only necessary for the study of stellar pulsations and SLF variability for massive stars in the SMC, but also provides a valuable complementary data set for the BLOeM project to supplement spectroscopic studies.

In this paper, we describe a novel software tool to extract high-quality light curves of massive stars in the SMC using data from the NASA Transiting Exoplanet Survey Satellite (TESS; Ricker et al. 2015) in Section 2. These light curves allow for the classification of different types of variability, such as coherent pulsations, SLF variability, stars with rotational modulation caused by spots, and binarity, which we describe in Section 3. In section 4, we study SLF variability in low-metallicity massive stars of the BLOeM sample, and we conclude in Section 5.

2 TESS LIGHT CURVE EXTRACTION

2.1 Sample selection

The BLOeM campaign provides a sample of 925 massive stars in the SMC (Shenar et al. 2024), which are useful for this work. This sample consists of main sequence (OB-type) and evolved (OBAF-type) massive stars, with masses ranging from about 7 to 60 $M_{\odot}$ and Gaia G-band magnitudes ranging from 10.1 down to 16.4. The HR diagram of the full BLOeM sample is presented in Fig. 1 using the parameters from Crowther & Bestenlehner 2025 and when available the revised parameters determined by Bestenlehner et al. 2025. The location of the BLOeM sample on the sky is shown in Fig. 2, which also indicates the stars with new PSF light curves extracted in this work (see Section 3).

2.2 The TESS mission and data

In this work we use time-series photometry assembled by the TESS space mission (Ricker et al. 2015; Ricker 2021a). TESS is a full-sky survey launched in 2018 with a primary goal to detect the transits of exoplanets orbiting bright stars in our Galaxy, but these data also allow for high-precision asteroseismic studies of massive stars (see e.g. Bowman et al. 2019a; Burssens et al. 2020, 2023). TESS is currently in its second extended mission and has to-date delivered light curves spanning several years for millions of stars across the sky. With particular attention to extracting SMC light curves with minimal contamination, the limiting magnitude is about 15 mag for TESS, which corresponds to roughly to masses above about 10 $M_{\odot}$ on the main sequence in the SMC (see Bowman et al. 2024). This approximate brightness limit of TESS in the HR diagram is shown as a red-dashed line in Fig. 1. Therefore, due to the specifications of the TESS mission, extracting reliable photometry is only possible for sufficiently bright and isolated BLOeM targets.

The reduced full-frame image (FFI) data from the TESS mission are publicly available (Jenkins et al. 2016; Ricker 2021b) from the MAST archive[1]. With the Lightkurve (Lightkurve Collaboration et al. 2018a) and TESScut (Brasseur et al. 2019) `python` packages, we searched for a target's coordinates, and downloaded a cut-out of the FFI centred on a target. Typically, cut-outs of at least 19×19 pixels[2] are needed to capture all the target signal as well as sufficient background pixels for background subtraction as part of the reduction procedure.

Simple aperture photometry (SAP) is the standard approach to extract a light curve from TESS FFI data. This is done with a so-called binary aperture pixel mask, such that pixels are assigned to either capture the target flux or not. The total flux is then the sum of the flux of all pixels in the selected aperture mask for each time stamp. The aperture mask is typically defined as consisting of pixels that contain flux above a certain threshold chosen based on the level of contamination and background around the target. See, for example, Bowman et al. 2022 and Garcia et al. 2022 for applications of SAP to TESS data for early-type stars. This is a sufficiently good approach for bright, well-isolated Galactic stars (see discussion by Scott & Bowman 2026), but starts to fail for fainter stars in more crowded regions. This is because the light of multiple nearby stars blends together in crowded regions, such as the SMC, meaning it becomes non-trivial to define an aperture mask without large amounts of contamination. Moreover, it becomes challenging to identify which signal (e.g. pulsation mode frequency) originates from which star. In a minority of cases, one could tackle the issue of contamination by only looking at the light curve of a single pixel in which the flux of the target of interest may dominate (e.g. Higgins & Bell 2023; Pauli

[1] https://archive.stsci.edu/missions-and-data/tess
[2] An odd number was chosen to conveniently define fixed SAP masks around the central pixel.

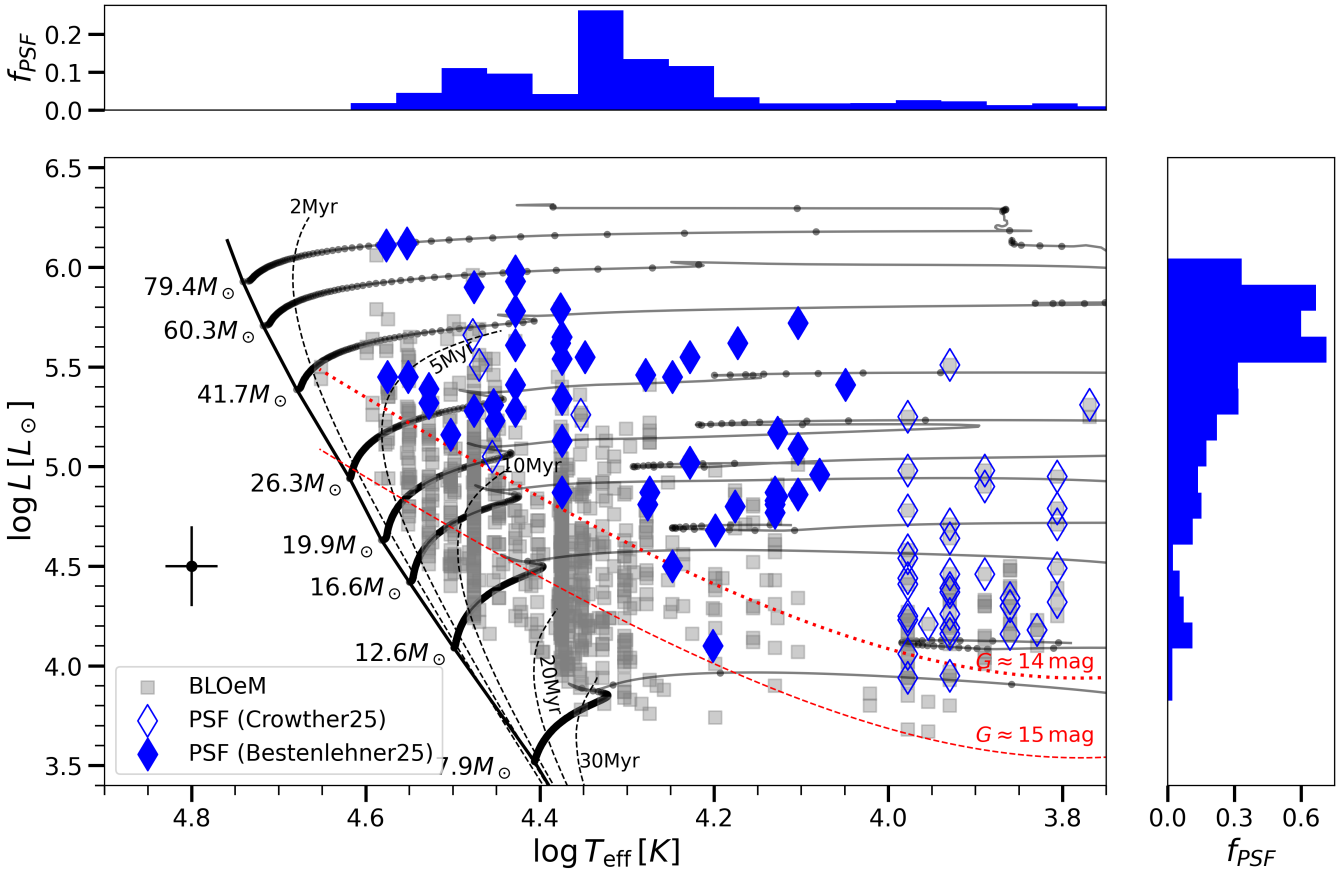

Figure 1. The locations in the HR diagram of all BLOeM targets (Shenar et al. 2024) are shown in grey using parameters from Bestenlehner et al. 2025 and Crowther & Bestenlehner 2025. The targets with successful PSF TESS light curves extracted are overplotted as blue diamonds. These have a slight bias towards the brighter and therefore more evolved part of the sample. This is delimited by the TESS brightness limit of about $G < 15$ mag, indicated by the red-dashed line. The histograms along each axis show the completeness fraction (i.e. the ratio of targets with PSF light curves relative to the number of total BLOeM stars in that bin for each axis). A typical error bar for the BLOeM spectroscopic parameters is shown in the bottom-left, as well as evolutionary tracks and isochrones from Schootemeijer et al. 2019.

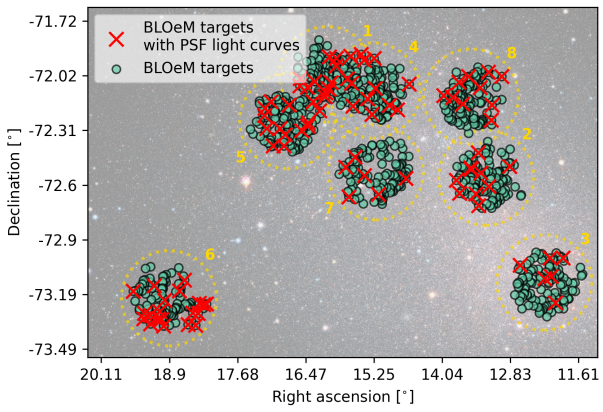

Figure 2. Spatial location of the targets for which a successful PSF light curve have been extracted. Figure adapted from Shenar et al. 2024.

et al. 2023), but this is more susceptible to unwanted pixel-to-pixel sensitivity and instrumental trends.

In this work, we have developed a novel light curve extraction software package called Lemons[3] that models how the light of a point source is distributed over a TESS FFI image — the point spread function (PSF). Our approach achieves a preferable balance between minimised flux contamination while incorporating as much astrophysical signal from the target star as possible in crowded regions. Our PSF approach is more robust against contamination compared to the commonly used SAP methodology because the pixels closer to a star's location on the CCD are prioritized when using a PSF approach, thus they contribute a higher weighted fraction in extracting a target's light curve. We show a 1D schematic of a Gaussian-like PSF in Fig 3, which demonstrates its advantages to the SAP approach for close sources.

PSF fitting of TESS TPF images to extract light curves is certainly not a new idea and has been done for studies targeting low-mass stars in the galaxy by Feinstein et al. 2019, Nardiello et al. 2019 as well as Han & Brandt 2023. However their tools are optimised for exoplanet searches and therefore often include light curve post processing techniques that potentially modify stellar variability. Therefore, after initial testing of available software tools specifically for extra-galactic massive stars (see Bowman et al. 2024), we have developed a new software tool better suited for studying massive

[3] https://github.com/pieterjanv314/psfv

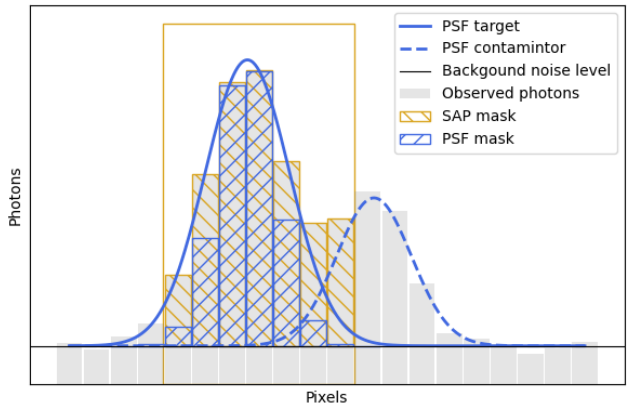

Figure 3. 1-dimensional schematic of PSF fitting on top of a background flux, applied on two artificial targets that blend together. The golden hased area represents a typical SAP mask, that in this example also captures contaminated signal.

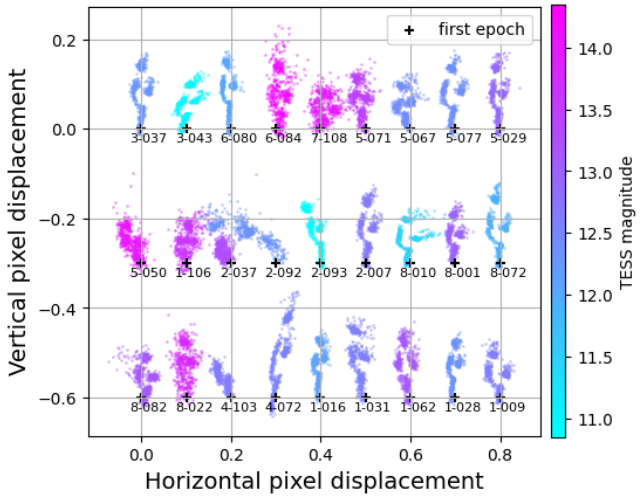

Figure 4. The relative path of the centroid for sector 68 of several SMC massive stars, each labelled with their BLOeM identifier and colour-coded with the stars TESS magnitude. The 1σ errors on these centroid positions are typically $0.05 \sim 0.1$ in terms of the pixel size. Each star is labelled by its BLOeM identifier.

star variability. Our approach has the advantages of including centroid tracking informed by ultra-precise co-ordinates assembled by ESA's Gaia mission (Gaia Collaboration et al. 2016, 2021, 2023), as well as accounting for variations in the size of the PSF per image frame, which is necessary for variable stars with large peak-to-peak variability (e.g. eclipsing binaries and high-amplitude pulsators).

2.3 Implementation of point spread function fitting

The Lemons code developed in this work makes use of the psf module within the photutils package (Bradley et al. 2022), which contains tools for PSF photometry. It performs a least-squares fit of 2D Gaussian PSFs, on top of an estimated background level with a Levenberg-Marquardt algorithm. This algorithm optimises parameters β, consisting of a height (amplitude), position (i.e. centroid) and broadness parameter, to minimise the χ^2 cost function

$$\chi^2(\beta) = \sum_i [f_i - (G_i(\beta) + b)]^2 \quad (1)$$

where i enumerates all pixels in the image, f_i and $G_i(\beta)$ represent the measured flux and the one predicted from the Gaussian PSF, respectively. Allowing centroid and broadness to be free parameters is key to our optimisation for variable stars. The background flux b is estimated as the average flux of all pixels fainter than 1 per cent of the median flux of the image excluding pixels containing sources. Relatively large TESS FFI cutouts of 19×19 pixels are used to ensure that sufficient background pixels are included. The final flux of a star in an image is extracted as the weighted sum over the pixel flux value, where different weights are assigned to each pixel according to the Gaussian PSF shape integrated over the pixel's area.

In our initial testing, we found that differences in the optical path for stars at different locations in the CCDs across all four TESS cameras as well as variable scattered light mean that the PSF of a target is both time and spatially dependent (Van Daele 2023) — see also discussion by Han & Brandt 2023. However, the tests performed by Van Daele 2023 illustrated that the assumption of circularly symmetric PSFs are sufficient for studying massive star variability given the relatively large pixel size (21 arcsec) of the instrument. In the case of variable scattered light, as long as the star is not too close to the edge of a CCD such that sufficient nearby background pixels are available, spherically symmetric PSFs provide reasonable results.

2.3.1 *Optimisation for stellar variability*

Our approach is optimised to study stellar variability in two main ways. Each represents a significant advantage to other open-source PSF-based light curve extraction tools currently available.

Firstly, the broadness (and amplitude) of the PSF is allowed to vary over time, which means that the full-width half-maximum (FWHM) of the Gaussian PSF is a free parameter. This is necessary because as an object becomes brighter, the light tends to spread out more on the detector. This is known as the 'brighter fatter' effect and occurs when a pixel receives enough electrons (due to the large number of incoming photons on the detector) that it influences the electric field locally, and causes electrons to spill over to neighbouring pixels (Howell 2006). Since massive stars are often variable in their light curves (see Bowman 2020), sometimes with peak-to-peak brightness variations as large as 1 mag on times scales of hours-to-weeks, the shape of the PSF must be allowed to vary in time.

Secondly, the centre of light, which represents the position of the star on the image, is also a free parameter for all TESS images. The Gaia space mission (Gaia Collaboration et al. 2016, 2021, 2023) has measured the precise locations of billions of stars, and we use these positions to precisely identify stars (i.e. BLOeM targets as well as contaminating stars) in TESS FFI images. However, the pointing of TESS and its world coordinate system is not as precise as Gaia's, hence it is a significant advantage to be guided by Gaia and allow the centroid to be a free parameter. Typically, the fitted PSF centroids in TESS FFIs deviate by about a tenth of TESS's 21-arcsec pixel size (corresponding to a few arcseconds on the sky) from the input Gaia position. Furthermore, there is an apparent movement of the PSF during each TESS sector because of drift and roll of the spacecraft, which is demonstrated in Fig. 4 for a typical subset of 27 SMC massive stars. The discontinuities in groups of points in Fig. 4 correspond to the data downloading gap that occurs near the middle of each TESS sector, in which the spacecraft points back towards Earth and then is re-pointed back on target. Naturally, this results in a different systematic pointing error both before and after the mid-sector data downlink. Furthermore, Fig. 4 illustrates that the PSF fitting of fainter stars is generally less precise in terms of centroid grouping,

and that stars in the same sector typically have similar x- and y-axis displacement patterns, which demonstrates how this effect is mainly instrumental in origin.

Importantly, our tests revealed that it is not advisable to assume a fixed location for a PSF using the Gaia location nor a target's average location, because flux enters and leaves a fixed-centroid Gaussian over time due to instrumental drift and therefore could introduce slow trends the extracted light curve. This is also true for the SAP approach when only a single pixel is used. Therefore, including the PSF centroid as a free parameter in all fits to the TESS image data, whilst providing the Gaia location as an initial guess, is crucial in order to obtain high accuracy for the resultant extracted light curves. For these reasons, it is advantageous for the PSF centroid and broadness to be free parameters.

We note that star-specific deviations from the general trends seen for the centroid locations of all stars shown in Fig. 4 could be caused by: (i) high proper motion stars; (ii) potential wobbling in the centre of light for an astrophysical reason (e.g. the changing light ratio between primary and secondary stars in an eclipsing binary system during the orbital phase); or (iii) rotational modulation, non-radial pulsations, and/or convective granulation changing the flux distribution on the surface of a star (see e.g. Chiavassa et al. 2011). We do not rule out any of these effects, except for the granulation since this typically occurs in red (super)giant stars and are not present in our sample, we do not find any clear evidence for any astrophysical cause of the scatter in Fig. 4 in our analysis. This is likely because such effects are much weaker than other instrumental sources of scatter in TESS image data. For example, we cross matched the measured x- and y-pixel centroid displacement patterns of all our stars with known high-proper motion stars and found no correlation. Moreover, stars with larger or atypical deviations in their measured centroids generally have larger centroid uncertainties and correspond to stars with fainter TESS and Gaia G-band magnitudes, making it challenging to infer any astrophysical origin.

2.3.2 *Limitations*

The nature of a PSF-based approach, specifically that the flux of a target is extracted based on a 2D weighting function, means that not all of the flux of a source is necessarily utilised. This means that PSF-extracted light curves tend to include larger relative fractions of Poisson noise relative to SAP light curves. Primarily, this is due to smaller number of photons being used in PSF fitting of crowded sources compared to SAP light curves with large aperture masks. The smaller average fluxes in PSF light curves can be thus more susceptible to read-out noise and instrumental effects, including intra-pixel effects. In general, a SAP light curve with a larger aperture mask tends to average out systematic effects at the cost of increasing contamination (see Pápics et al. 2017). Whereas a PSF light curve reduces contaminated signal and follows the centroid of the PSF more accurately, at the cost of potentially introducing trends from the pixel-to-pixel sensitivity. Because this depends on the CCD properties of the region around the target, it is advisable to compare the light curves from both techniques for crowded regions.

A second major limitation of our PSF approach is that it may return unreliable results for (very) faint stars (i.e. $G \gtrsim 15$ mag), regardless of whether they are contaminated or not, since such stars are of similar brightness to the background in a TESS image. However, in practice this depends on a specific star's crowding and the time- and spatially dependent scattered light in TESS FFI data. Under these conditions, the fitting of a (very) faint star typically returns unrealistically high PSF broadness values, often extending beyond the image boundaries. Note that this limitation is set by the specifications of the TESS instrument rather than the PSF extraction technique itself, as we are pushing TESS mission data far beyond what it was originally designed to provide. Unfortunately, these criteria for faint stars yields an empirical brightness limit of approximately $G \gtrsim 15$ mag for stars in the SMC. This means that the majority of the BLOeM sample of SMC massive stars are not feasible for extracting reliable PSF light curves (see also Section 3).

2.4 Results and example case studies

After extensive testing and implementation, a sub-sample of 91 BLOeM targets have good quality TESS PSF light curves, which are indicated in Figs. 1 and 2. Although they comprise only about 10 per cent of the full BLOeM sample, it is a much larger sample than Bowman et al. 2024 and spans a variety of stellar masses and evolutionary stages. For the remainder of the stars, we also extracted SAP light curves using standard 3×3 aperture masks and provide these as a data product. However, we caution that such light curves are heavily contaminated and should not be analysed blindly.

Here we demonstrate the advantage of our PSF approach compared to SAP methods using example stars within the BLOeM sample of massive stars in the SMC. In each example of specific scenarios, we compare the SAP and PSF light curves and demonstrate the effectiveness of the PSF methodology.

2.4.1 *GAIA DR3 4690516677131714432: False positive eclipsing binary*

Figure 5 shows the light curve of GAIA DR3 4690516677131714432 (BLOeM 4-058; Sk 80), a ~ 60 $M_\odot$ O7Iaf$^+$ giant star (Shenar et al. 2024; Bestenlehner et al. 2025). The SAP light curve of this star reveals SLF variability, higher frequency coherent pulsations as well as eclipses caused by a binary companion. However, the PSF light curve for this star, and its close neighbour, effectively disentangles all of these signals and successfully attributes the eclipses to the contaminating star and not the BLOeM target of interest. We identify the contaminating signal to come from GAIA DR3 4690516883290136832, a star outside the BLOeM sample. It is worth noting that the contaminating star is about 6 times brighter than our target of interest. This illustrates the importance of our PSF method because SAP light curves of massive stars can easily lead to false positive eclipsing binary systems (see Abdul-Masih et al. 2016; Prša et al. 2022). This is especially important for massive stars in the LMC and SMC, because of the (moderate-to-severe) crowding, as can be seen in the TESS CCD image in the top panel of Fig. 5.

2.4.2 *GAIA DR3 4688967568356557440: PSF light curve of an isolated constant star*

The jitter in addition to the systematic movement of the PSF centroids of all BLOeM stars (cf. Fig. 4) have an uncertain origin and could be caused by both astrophysical and/or instrumental effects, as discussed in Section 2.3.1. This could be a point of concern, since no artificial variability should be introduced into a light curve caused by centroid jitter.

To verify the impact of centroid jitter in a PSF light curve, we compare the SAP and PSF light curve for a constant star, GAIA DR3 4688967568356557440, in Fig. 6. This example demonstrates that having the PSF centroid as a free parameter in the fit does not introduce additional non-astrophysical variability in the light curve.

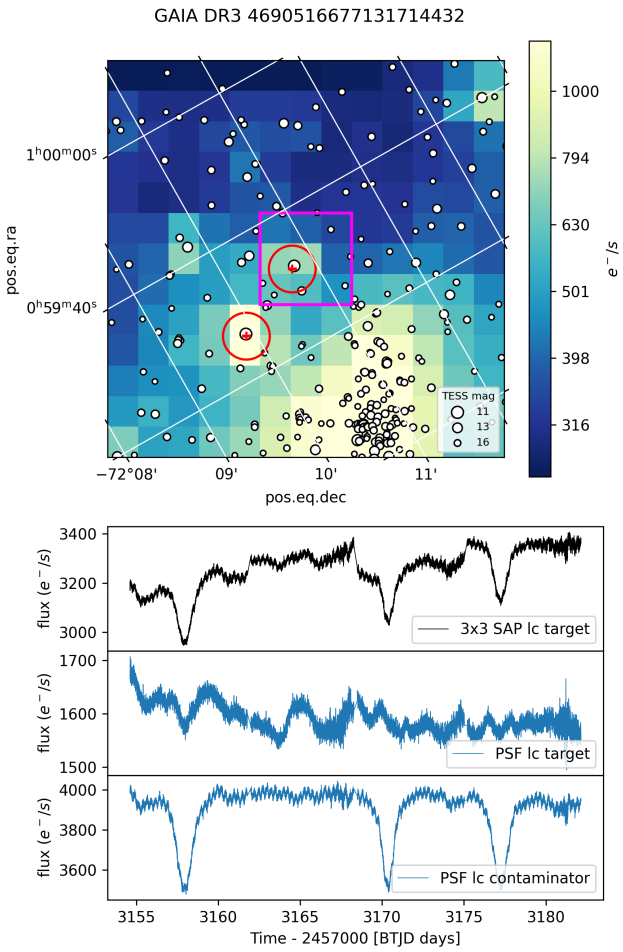

Figure 5. Demonstration of successfully disentangling contamination to reveal a false positive eclipsing binary. Upper panel: TESS pixel image around GAIA DR3 4690516677131714432. The red circles indicate the FWHM of the Gaussian PSF fit and the magenta rectangle illustrates a standard 3 × 3 SAP mask. Lower panels: SAP (black) and PSF (blue) extracted light curves of GAIA DR3 4690516677131714432 as well as the PSF light curve of contaminating stars. The SAP light curve is a combination of multiple sources of variability whereas the PSF light curves effectively disentangle them.

Moreover, a decreasing trend and jumps are present in the SAP light curve which do not occur in the PSF light curve. Since both light curves are not detrended and underwent the same background subtraction, this difference arises solely from the telescope drift and slight differences in pointing before and after the mid-sector data downlinking of the TESS spacecraft. In our PSF approach, this is mitigated by allowing for centroid freedom in the PSF fit. Whereas, in the SAP light curve extraction, a changing fraction of photons are being captured by the aperture mask, which is fixed in terms of pixel location. This example therefore also illustrates the advantage of a optimised flexible aperture mask in the PSF fitting approach.

2.5 TESS and OGLE comparison

OGLE is a long-term ground-based observational campaign program that assembles time-series photometry of galactic, LMC, and SMC stars (Udalski et al. 2015; Soszyński et al. 2023). Although OGLE is unable to match TESS's photometric precision, nor its high duty cycle and short cadence, its smaller pixel size and observing strategy allows

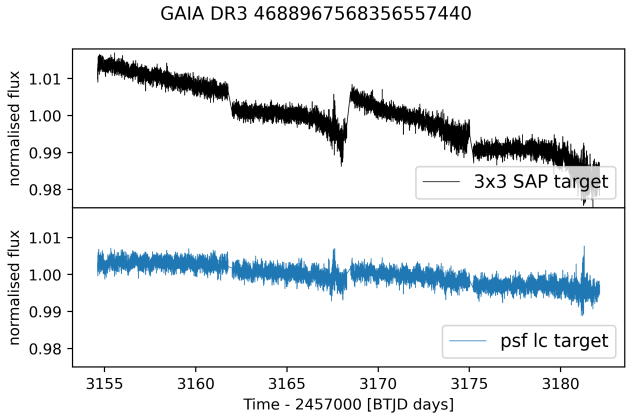

Figure 6. Demonstration of similar noise properties (i.e. jitter) between the 3 × 3 SAP light curve and the PSF light curve in TESS sector 68 for GAIA DR3 4688967568356557440.

for a much higher spatial resolution and long base lines of several years. This means that OGLE photometry is entirely complementary to TESS light curves.

As a sanity check on the performance of our PSF fitting approach we compared our extracted TESS light curves to OGLE light curves of known variable stars. Figure 7 shows a comparison of TESS and OGLE light curves for two binary systems in our sample, which are phase folded on the OGLE extracted binary period. The period recovery is excellent, and the scatter is similar. This demonstrates that our PSF method indeed captures the astrophysical signal from the target of interest within the crowded TESS data.

3 PHOTOMETRIC VARIABILITY OF SMC MASSIVE STARS IN THE BLOEM SAMPLE

PSF fitting of TESS FFIs was attempted for a subsample of 226 massive stars from the BLOeM project, which is all of the stars with Gaia $G < 15$ mag and the ratio of the target's flux, relative to the total flux of all stars (from the TESS Input Catalogue) within a 21 arcsec radius, is more than 50 per cent ($F_*/F_{21\mathrm{arcsec}} > 0.5$). In other words, stars that are too faint to be observed with TESS and/or stars for which crowding is too severe were excluded. This is based on our initial tests and because our current methods do not allow for the PSF light curve extraction of such extreme cases (see also Section 2.3.2).

PSF fitting was attempted on this subsample of 226 stars (see Section 2.1), and PSF light curves were successfully extracted for 91 stars, with a total of 281 light curves of individual sectors. Although this is a relatively small percentage of the total BLOeM sample, each individual light curve is an accomplishment considering that this technique pushes the possibilities of what was thought achievable with TESS mission data — the instrument was not designed to study SMC stars. In this faint and crowded regime, the success of PSF fitting depends largely on the brightness ratio and local image geometry (i.e. location of stars on the 2D sky projection on the CCD) of the target with respect to nearby stars in the CCD image. The PSF approach typically starts to fail for stars with $13 \lesssim G \lesssim 14$ mag and/or $F_*/F_{42\mathrm{arcsec}} \leq 0.4$. However, in cases with little contamination, we have successfully reached the brightness limit of ~ 15 mag. Beyond this point, targets are indistinguishable from background noise in the TESS CCD images.

Because of the technical limitations of the TESS instrument, there

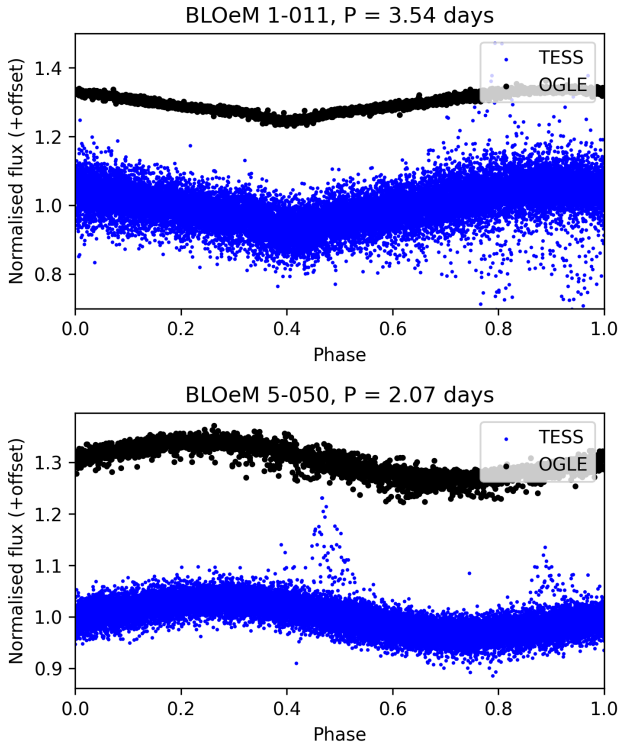

Figure 7. Comparison of PSF TESS and OGLE light curves to two known binaries. The top and bottom panels show the phase folded OGLE (black, with offset) and PSF TESS (blue) light curves for BLOeM 1-011 (GAIA DR3 4690506712804881792) and BLOeM 5-050 (GAIA DR3 4687501953697501568), respectively. The orbital period extracted from TESS and OGLE are within error and is indicated above each plot and is recovered robustly.

is a clear observational bias of being able to successfully extract a PSF light curve for intrinsically more luminous stars. Therefore, our sample with successful PSF light curves is dominated by main sequence O dwarfs (i.e. masses above $\sim$ 20 $M_\odot$) and post-main sequence stars (i.e. giants and supergiants). In the HR diagram in Fig. 1, the successfully extracted 91 stars are overplotted as blue diamonds. We also include histograms adjacent to the x- and y-axes that show the completeness of stars with a PSF light curves compared to the complete BLOeM sample as a function of $T_{\rm eff}$ and L, respectively.

Regardless of the relatively low success rate, our PSF light curves reveal several types of variability indicative of coherent pulsation modes excited by a heat-engine mechanism, eclipsing binaries, SLF variability, and rotational modulation caused by chemical spots (i.e. candidate magnetic stars), which are discussed in greater detail in the following subsections. We also provide a variability classification for each star with a successfully extracted PSF light curve in Table A1. As mentioned previously, for all 925 BLOeM targets, we also extracted 3×3 pixel SAP light curves for completeness, and provide a variability classification in Table **Appendix Table**.

3.1 Pulsations

The lower metallicity of the SMC means there is a weaker source of opacity in the iron-bump at 200 000 K, which is the excitation mechanism for coherent pulsation modes in massive stars (Dziembowski & Pamyatnykh 1993). Therefore, it is expected that fewer, if any, coherent heat-driven pulsating massive stars exist in the SMC (e.g. Salmon et al. 2012). However, Be stars, for which pulsations can be triggered by their fast rotation rates, are more likely to exhibit coherent pulsations than ordinary B-type stars, despite the low metallicity environment. (see Diago et al. 2008; Labadie-Bartz et al. 2022). On the other hand, IGWs are predicted by numerical simulations to be stochastically excited at the interface of convective and radiative zones (Rogers et al. 2013; Rogers & McElwaine 2017; Edelmann et al. 2019; Thompson et al. 2024), and inferred to be the cause of SLF variability in massive stars (Bowman et al. 2019a, 2020). IGWs are especially important to study in low-metallicity massive stars, since such stars may lack entirely sub-surface convection zones (Jermyn et al. 2022). This means that the observed SLF variability must arise from the convective core. For example, Bowman et al. 2024 found little difference in the morphologies of SLF variability across Galactic, LMC and SMC massive stars. Below we discuss two cases of pulsational variability: one star with coherent pulsations and one with SLF variability. We find a total of 14 coherent pulsators (candidates) and numerous examples of SLF variability in our sample of massive stars with PSF light curves, with the latter being discussed in more detail in Section 4.

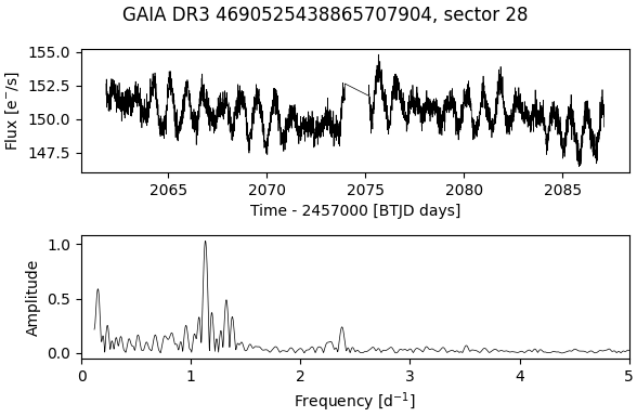

Figure 8. PSF light curve and Lomb-Scargle periodogram of GAIA DR3 4690525438865707904, which has coherent gravity-mode pulsations typical of an Oe/Be star.

3.1.1 *GAIA DR3 4690525438865707904: coherent heat-driven pulsations in an Oe/Be star*

GAIA DR3 4690525438865707904 (BLOeM 1-040) is an O9.7 III:ne star and a known SB1 system with an orbital period of approximately 45 d (Bodensteiner et al. 2025), which is longer than a single TESS sector. Our PSF light curve and the corresponding Lomb-Scargle periodogram for sector 28 are shown in Fig. 8.

We detect additional variability in our PSF light curve at a frequency of 1.13 d^{-1}. Since this star is an Oe/Be star, and such stars are commonly pulsators (see Labadie-Bartz et al. 2022), we conclude that this star has coherent heat-driven pulsations (see also Stankov & Handler 2005; Burssens et al. 2020). There is also a harmonic of the dominant frequency at 2.26 d^{-1}, which further supports this conclusion as frequency groups such as this are common in pulsating Be stars (see Kurtz et al. 2015; Labadie-Bartz et al. 2022).

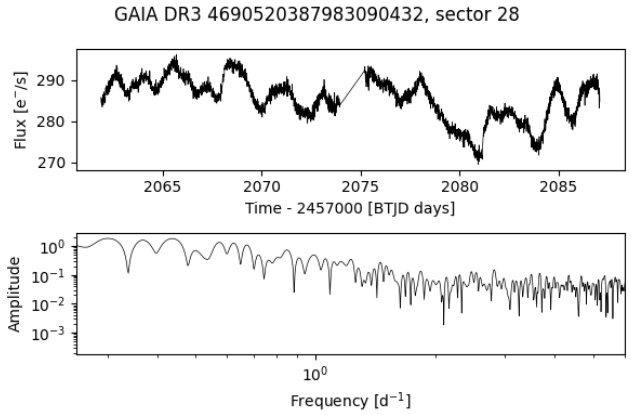

Figure 9. PSF light curve and Lomb-Scargle periodogram of GAIA DR3 4690520387983090432, which is a typical example of a massive star with SLF variability.

3.1.2 GAIA DR3 4690520387983090432: SLF variability

GAIA DR3 4690520387983090432 (BLOeM 1-009) is a B1 Ia type star (Britavskiy et al. 2025; Shenar et al. 2024) and its light curve is a typical example of massive star SLF variability. Our PSF light curve and the corresponding Lomb-Scargle periodogram for sector 28 are shown in Fig. 9, which clearly illustrate the quasi- and multi-periodic nature of SLF variability.

Additional difficulties can arise in analysing spectroscopic data of pulsating stars, such as those with SLF variability, since pulsations change the shapes of spectral lines and introduce significant radial velocity (RV) scatter (see Aerts et al. 2009; Aerts & Rogers 2015; Kalita et al. 2025). This star (and others like it) demonstrate the complementarity of using time-series photometry to quantify the contribution of RV variability caused by pulsations when interpreting multi-epoch spectroscopy to identify binaries.

3.2 Indications of binarity and rotation

Among the 91 BLOeM targets with successful PSF extracted TESS light curves, there are seven targets that show eclipses or ellipsoidal variability (EV), which are photometric signatures of binarity. It is often difficult to differentiate EV from rotational modulation, and impossible in a synchronised binary system without any extra information. However, finding a photometric variability period in agreement with a binary period found with BLOeM spectroscopy is therefore a strong confirmation of binarity. Unfortunately, from only the first 9 of 25 spectroscopic epochs in the BLOeM project, an unambiguous binary period has not yet been determined for most of these seven stars. Therefore, in this work we provide photometric periods to assist in solving the binary systems in the future when all 25 BLOeM epochs are available. The seven photometric binaries found in this work are provided in Table 1, and phase-folded TESS PSF light curves for each star are presented in Fig. 10. Below, we provide some comments on the individual targets.

3.2.1 GAIA DR3 4685947553531340800

GAIA DR3 4685947553531340800 (BLOeM 3-042, Sk 18) is a known O6 I(f)+O7.5 SB2 binary system (Shenar et al. 2024; Bestenlehner et al. 2025; Sana et al. 2025). However, no binary period has been determined to date. TESS photometry, shown in Fig. 10, reveals clear variability with a period of 1.16 d. This variability is more likely caused by rotational modulation rather than binarity owing to its short period.

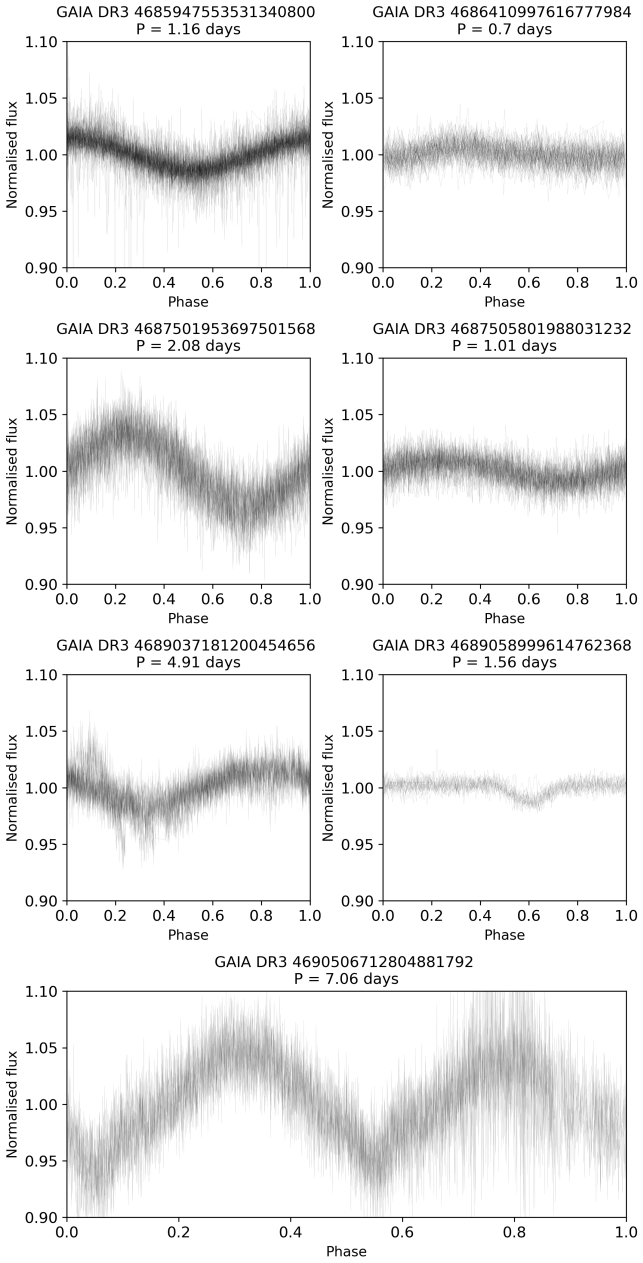

Figure 10. Phase-folded light curves of targets with potential binarity indications. The target name and the period, P, is mentioned in each subplot's title. The vertical axis has the same scale for all plots for comparison reasons.

3.2.2 GAIA DR3 4686410997616777984

GAIA DR3 4686410997616777984 (BLOeM 6-105) is a known SB1 type star, with spectral type O6 V:n (Shenar et al. 2024; Bestenlehner et al. 2025; Sana et al. 2025). No binary period has been constrained yet. Its light curve, see Fig. 10, shows a weak period of 0.7 d, which is very short for a massive binary, and so likely is caused by rotational modulation.

Table 1. Summary of stars with a PSF light curve extracted in this work that indicate potential binarity.

GAIA DR3 ID	SpT	TESS variability	BLOeM binary status	BLOeM binary period	PSF light curve period (d)
4685947553531340800	O6 I(f)	EV or RotMod	SB2	not yet in a paper	1.16 (or double)
4686410997616777984	O6 V:n	EV or RotMod	SB1	not yet in a paper	0.7 (?)
4687501953697501568	O9.7 V:	EV or RotMod	SB2	not yet in a paper	2.08 (or double)
4687505801988031232	B1.5 e	SLF (eclipses?)	–	–	1.01
4689037181200454656	B2.5 II-Ib	EV or RotMod (or SLF?)	SB1/LPV	0.82 days (Britavskiy et al. 2025)	4.91 ?
4689058999614762368	F0:	contaminated (EB?)	–	–	1.56
4690506712804881792	B1.5 II	EV or RotMod	SB2	7.07 days (Britavskiy et al. 2025)	3.54

3.2.3 GAIA DR3 4687501953697501568

GAIA DR3 4687501953697501568 (BLOeM 5-050) is a known O9.7 V: + early-B SB2 binary system (Shenar et al. 2024; Bestenlehner et al. 2025; Sana et al. 2025). However, no binary period has been determined yet. Our PSF TESS light curve, shown in Fig. 10, reveals variability with a period of 2.08 d, which could plausibly be either EV or rotational modulation.

3.2.4 GAIA DR3 4687505801988031232

This rapidly rotating B1.5 e type star (Shenar et al. 2024; Bestenlehner et al. 2025; Sana et al. 2025) (BLOeM 1-106) has photometric variability with a dominant period of 1.01 d. There is also a weaker 5-d period in the light curve, however we deem it to be likely arising from contamination since it is not present in the central pixel where one would expect the signal to be strongest if arising from the target of interest. Such a short period of 1.01 d is unlikely to be a binary period, so we infer this more likely to be rotational modulation.

3.2.5 GAIA DR3 4689037181200454656

For GAIA DR3 4689037181200454656 (BLOeM 8-006), which is a B2.5 II-Ib type star, BLOeM studies have found a spectroscopic period of 0.82 d (Britavskiy et al. 2025; Shenar et al. 2024; Bestenlehner et al. 2025; Sana et al. 2025). However, the periodogram of our TESS light curve does not reveal any significant peak at that frequency. Instead, we find a significant period of 4.91 d (see also Fig. 10), which is six times larger than the previously reported period of 0.82 d.

This target is the only one of the seven candidate binaries in our work for which the dominant photometric period is not in agreement with the binary period based on BLOeM spectroscopy. Assuming the BLOeM binary period is correct, this discrepancy could be caused by: (i) photometric contamination from nearby sources in the TESS CCD images leading to a false positive; and (ii) the variability detected in TESS photometry arises from rotational modulation rather than binarity in a non-synchronous system. Finally, it is also possible that the photometric signatures of the BLOeM binary period is too low in terms of S/N to be detected in our TESS light curves. On the other hand, the spectroscopic orbital period is very small for a massive star and our detected photometric period is a harmonic (i.e. six times larger). Therefore, we conclude that the TESS photometric period is the real orbital period and the 0.82-d period reported by Britavskiy et al. 2025 is an alias.

3.2.6 GAIA DR3 4689058999614762368

GAIA DR3 4689058999614762368 (BLOeM 8-097) is an F0: giant type star with unknown binary status (Patrick et al. 2025; Shenar et al. 2024; Bestenlehner et al. 2025; Sana et al. 2025). Its light curve, shown in Fig. 10, reveals weak, but regular eclipses with a period of 1.56 d. These shallow (and somewhat asymmetric) eclipses imply binarity. However, given such a short period and such an evolved star, this seems unlikely. On the other hand, this star has one of the lowest standard deviations for extracted RVs within the sample of Patrick et al. 2025.

With such a faint signal, extra caution is advised due to the risk of contamination. Indeed, when investigating the light curves of the individual TESS pixels, the signal appears to be stronger on a pixel next to the target, where four faint star are located ($16.5 < G < 18.0$ mag), compared to the target ($G = 13.8$ mag). Unfortunately, all these stars are too faint to be captured within the PSF. However if one of them has a very strong variability, this could still enter the targets light curve. Hence, we deem the eclipses to be potential contamination.

3.2.7 GAIA DR3 4690506712804881792

GAIA DR3 4690506712804881792 (BLOeM 1-011) is a known SB2 system, with a primary star of spectral type B1.5 II and binary period of 7.07 d (Britavskiy et al. 2025; Shenar et al. 2024; Bestenlehner et al. 2025; Sana et al. 2025). The strongest period in the TESS light curve, shown in Fig. 10, and Lomb-Scargle periodogram is 3.54 d. This is half of what was found with BLOeM spectroscopy, a strong confirmation that we are observing the same signal. We opted to phasefold this light curve using the BLOeM period in Fig. 10. Assuming that 7.07 d is the true binary orbital period, the symmetry of the two dips in the phase folded light curve suggests that this is a low-eccentricity binary systems with stars of similar brightness.

4 SLF VARIABILITY AT SMC METALLICITY

In addition to the study of coherent pulsators and binary systems, these new PSF light curves allow us to investigate the nature of SLF variability in SMC stars and how its morphology correlates with stellar parameters, in particular the location in the HR diagram. Moreover, since almost all studies of SLF variability to date have been for galactic stars, in this case we can study massive stars in the SMC, and determine the impact of metallicity on SLF variability. We explore this topic by mapping the observed SLF variability for our subsample of stars with extracted PSF light curves, compare the results with what has been found previously for galactic stars and

investigate any difference in SLF morphology among main-sequence and post-main sequence stars.

The most common approach to study SLF variability is to fit the periodogram (see review by Bowman 2023), but other methods include fitting the light curve directly using Gaussian process regression (see Bowman & Dorn-Wallenstein 2022). Inspired by the original large sample studies of Bowman et al. 2019a and Bowman et al. 2019b, we use a semi-Lorentzian function to fit the periodogram with least squares and characterise the maximum amplitude α_0, characteristic frequency, $\nu_{\rm char}$, and steepness, γ, on top of a white noise level $C_{\rm w}$ using:

$$\alpha(\nu) = \frac{\alpha_0}{1 + \left(\frac{\nu}{\nu_{\rm char}}\right)^{\gamma}} + C_{\rm w} \ . \tag{2}$$

Light curves with significant periodicity (pulsations or eclipses) have been iteratively prewhitened with Period04 (Lenz & Breger 2005) to remove their dominant peaks in the periodogram as this would prevent a successful fitting. An example of this is shown in the left-hand panel of Fig. 11. The resultant profiles of SLF variability are for periodograms of light curves spanning a single sector, since the large data gap in between TESS sectors would introduce an artificial excess at low frequencies in the periodograms. When multiple consecutive sectors are available of the same star, their light curves are treated as independent observations, but all underwent the same process separately.

Most stars were observed for several sectors, but not all of the sectors have suitable PSF light curves to fit their SLF variability. Several stars have some sectors dominated by instrumental effects, such as data gaps, and residual time-dependent scattered light, which our PSF-based approach to extracting light curves attempts to mitigate but is not perfect. These problematic light curves are often flagged by the TESS mission pipeline. Such instrumental effects cause an additional excess at very low frequencies (i.e. $\nu < 0.1$ d^{-1}), resulting in a periodogram that keeps increasing towards lower frequencies and does not plateau at a discernible value of α_0. An example of expected behaviour is shown in the bottom panel of Fig. **??**. However, in the cases when instrumental effects dominate astrophysical variability, it is difficult to reliably measure the properties of the SLF variability. Therefore, we filtered out stars with fitted SLF variability profiles with $\nu_{\rm char} < 0.15$ d^{-1}. An example of this behaviour is shown in the middle panel of Fig. 11. This is motivated by the fact that such small frequencies cannot be resolved in a single sector of TESS data because its resolution is the inverse of the time span. Based on this, we filtered out 139 sectors of light curves for 72 stars. Finally, after a visual inspection of the quality of the fits, we removed a further 17 sectors of light curves because the fitted SLF variability model clearly did not match the data. An example of a poorly fit star is shown in the right-hand panel of Fig. 11.

After this filtering process, we are left with 105 sectors for 51 massive stars, for which there is a high degree of confidence that the SLF variability is astrophysical. For all of these stars, the Bayesian Information Criterion (BIC; Schwarz 1978) was used to check that best fitted Lorentzian profile (cf. Eqn 2) is statistically preferred over the simpler model of a horizontal line (i.e. zero gradient white noise only).

Following Bowman et al. 2024, we show HR diagrams of all stars with significant SLF variability in Fig. 12, which have been colour-coded by $\nu_{\rm max}$ in the left panel and colour-coded by the SLF variability amplitude relative to the white noise limit (i.e. $\alpha_0/C_{\rm w}$) in the right panel. This demonstrates that SLF variability is common among different masses and evolutionary stages for SMC massive stars. We also determine the (lack of) correlations between $\nu_{\rm char}$ and α_0 with $\log(L)$, $\log(T_{\rm eff})$ using weighted linear regressions, which are shown in Fig. 13, in which multiple sectors per star are utilised. The weights on the data points are determined by the uncertainties on the fitted SLF variability parameters $\nu_{\rm char}$ and α_0. Significance of each pair-wise correlation is judged used p-values in which the null hypothesis is that there is no correlation between two parameters.

The regression statistics indicate a strong significant anti-correlation between $\nu_{\rm char}$ and $T_{\rm eff}$, as well as a strong significant correlation between luminosity and $\alpha_0/C_{\rm w}$. In other words, more luminous stars have stronger SLF variability, and cooler (i.e. more evolved) stars have longer period SLF variability. However, we find no statistically significant correlation between $\alpha_0/c_{\rm w}$ and $T_{\rm eff}$. These trends for SMC stars are largely in agreement with what was found for Galactic massive stars by Bowman et al. 2020. On the other hand, Bowman et al. 2020 found a correlation of larger α_0 with lower $T_{\rm eff}$, but this is not significant in our sample. We surmise this is possibly due to the lack of stars close to the ZAMS in our sample, since the vast majority of all BLOeM stars with PSF light curves showing SLF variability are near or beyond the TAMS (see Fig. 12). Nevertheless, the similarities between the SMC sample in this work and the galactic sample of massive stars of Bowman et al. 2020 suggests that the underlying excitation mechanism of SLF variability must be largely independent of a star's metallicity.

We emphasise that the R^2 values of all linear regressions shown in Fig. 13 are all < 0.2, which implies that the location in the HR diagram alone is not sufficient to predict a star's SLF variability profile. This is because the the sector-to-sector scatter in the SLF variability morphology parameters is quite large, which adds significant scatter in all regressions. Furthermore, what is also not captured in such a small sample of stars is the impact of binarity, differing rotation rates, or magnetic fields, which could all influence the SLF variability parameters, in addition to location in the HR diagram.

To investigate whether there is a difference in SLF variability morphology across different evolutionary stages, we divided our sample in two subgroups based on their luminosities: (i) higher luminosity stars (i.e. $\log(L/L_\odot) > 5.1$) which is also typically high-mass (i.e. $M \gtrsim 20\ M_\odot$) and mostly main-sequence stars as indicated by the blue shaded region in Fig. 12; and (ii) lower-luminosity stars mainly consisting of post-main sequence lower-mass stars ($8M_\odot < M \lesssim 20\ M_\odot$), as indicated by the green region in Fig. 12. Both subsamples underwent independent linear regressions and an F-test for comparing nested linear regression models (see e.g. Boussiala 2020) was performed, with the results shown in Fig. 14. The most apparent difference between the two subsamples is that, on average, the higher luminosity stars have higher SLF variability amplitudes, which was also seen for Galactic massive stars by Bowman et al. 2020. Interestingly, an important new result from our work is that the F-test supports the conclusion that separate models are required to treat each subsample when SLF variability amplitudes are plotted against $\log(L)$. Additionally, we conclude that $\log(\nu_{\rm char})$ transitions relatively linearly as stars evolve beyond the TAMS in the Hertzsprung gap for SMC massive stars.

The discrepancy of SLF variability amplitudes in both subsamples can be interpreted considering the mass difference between the two subsamples rather then their different evolutionary stages. Higher mass stars have larger (convective core) luminosities thus can allow for higher amplitude pulsations. This also explains the relative steep gradient in the $\log(\alpha_0/C_w)$ versus $\log(L)$ plot in Fig. 14 for the high-mass subsample. This is because in this region of the HR diagram, evolutionary tracks are mostly horizontal meaning that luminosity serves as a proxy for stellar mass. Of course, expand-

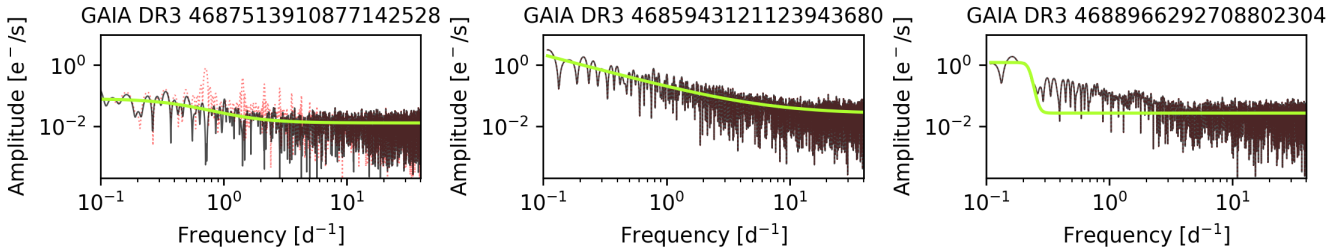

Figure 11. Example fitted SLF variability profiles for different stars. Left panel: example of a star that underwent prewhitening, with the original and residual periodograms shown in red and black, respectively. Middle panel: Fitted SLF variability profile that has been excluded form further analysis because $\nu_{\rm char} < 0.15\ {\rm d}^{-1}$. Right panel: Example of SLF variability with a poorly fitted profile and hence excluded from further analysis because of the visual discrepancy between the fitted curve and periodogram.

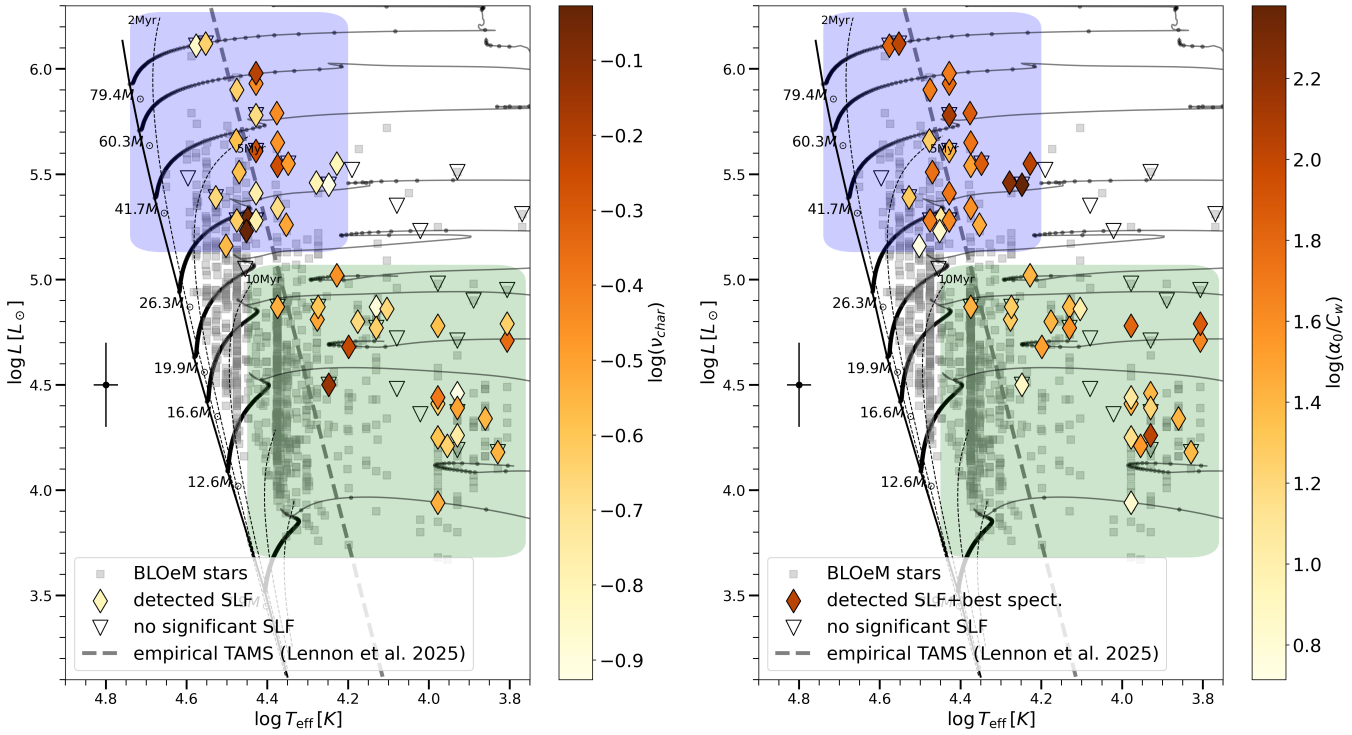

Figure 12. Location in the HR diagram of the 51 massive stars with significant SLF variability shown as diamonds, which are colour-coded by the characteristic frequency and amplitude relative to the white noise level of their SLF variability in the left and right panels, respectively. When multiple sectors for a star are available, the values shown correspond to the most recent sector available. The gray dashed line is the empirical location of the TAMS based on a decrease in the average v sin i value for the BLOeM sample from (Lennon et al. 2025). The sample is further divided in a high-mass main sequence subsample (blue region) and lower mass, mostly post-main sequence stars (green region).

ing both subsamples to include low-mass main-sequence stars and evolved high-mass stars would help further in breaking degeneracies between mass and age. However, high-mass post-main sequence stars, are rare due to their fast evolving nature. This is especially true for stars with birth masses of $M \gtrsim 40\ {\rm M}_\odot$ because they are subject to the Humphreys-Davidson limit (see Humphreys & Davidson 1979). The lack of lower-mass main-sequence stars in our sample corresponds with the limiting brightness we can observe in the SMC with TESS. Nonetheless, such trends would also prove interesting for galactic massive stars.

Regardless, our sample is sufficient to illustrate the common and diverse nature of SLF variability within SMC massive stars. Our data shows clear indications that the morphology of SLF variability correlates with different physical properties of the stars, such as stellar mass. However, there is a lot of room for further investigation, exploring the role of rotation, binarity, and chemical mixing, and how these contribute to scatter in the inferred parameters.

5 CONCLUSIONS

In this work, we have developed a new software tool, Lemons, to extract light curves by modelling PSFs of a sample of massive star targets and minimise contamination from nearby sources in TESS FFI images. Our PSF fitting software tool is optimised for massive stars, which are often variable with a large range of periods and

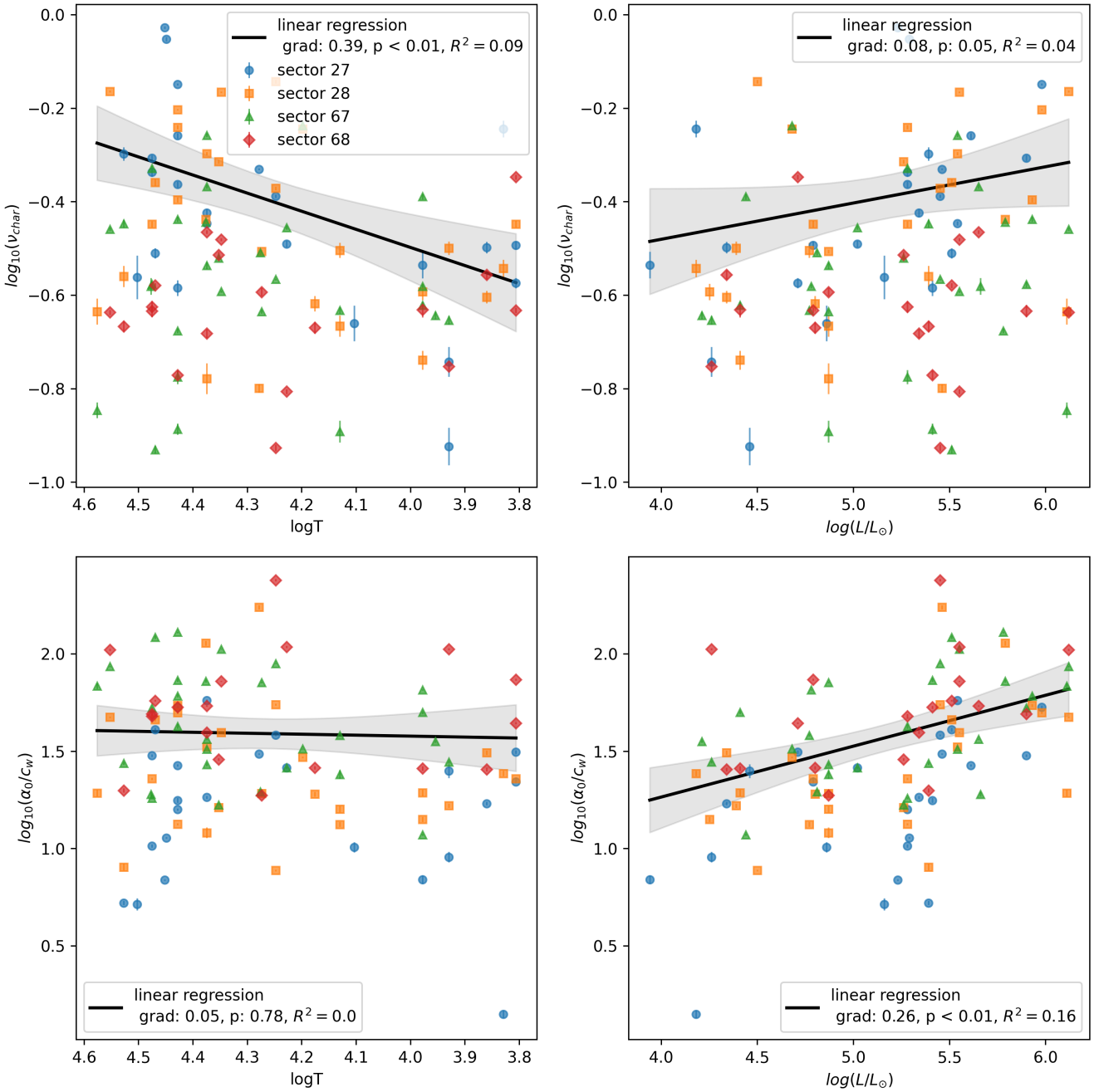

Figure 13. Overview of SLF variability parameters as a function of $T_{\rm eff}$ and luminosity. The different colours indicate the different sectors that have been used to calculate the SLF variability parameters as shown in the legend of the upper left panel. A weighted linear regression combining all sectors is also shown in black, together with a 95% confidence interval. The gradient and p-value of these regressions are provided in each panel's legend.

amplitudes, hence require flexibility to extract optimal light curves. For example, we demonstrate that PSF centroid and broadness as free parameters yield superior light curves. We illustrate that this method mitigates contamination issues, compared to the standard simple aperture photometry, in particular for faint ($\sim 13-15$mag) targets and stars in crowded regions for a sub-set of the BLOeM massive stars in the SMC.

We provide a new sample of 91 massive SMC stars with TESS light curves, along with a variability classification. In these low-metallicity stars, we observe different types of variability, including coherent pulsators, binarity, rotational modulation, and SLF variability. Our light curves also show that SLF variability is common in massive stars in the SMC and that it has a similar morphology to massive stars in the LMC and Milky Way galaxies. Given the weaker or absent subsurface convection zones for these stars because of the significantly lower metallicity, we conclude that SLF variability cannot solely be triggered by sub-surface convection.

When combined with the ongoing BLOeM spectroscopic survey of the SMC, these PSF light curves allow ensemble studies for binarity and pulsations in low-metallicity massive stars. Asteroseismology

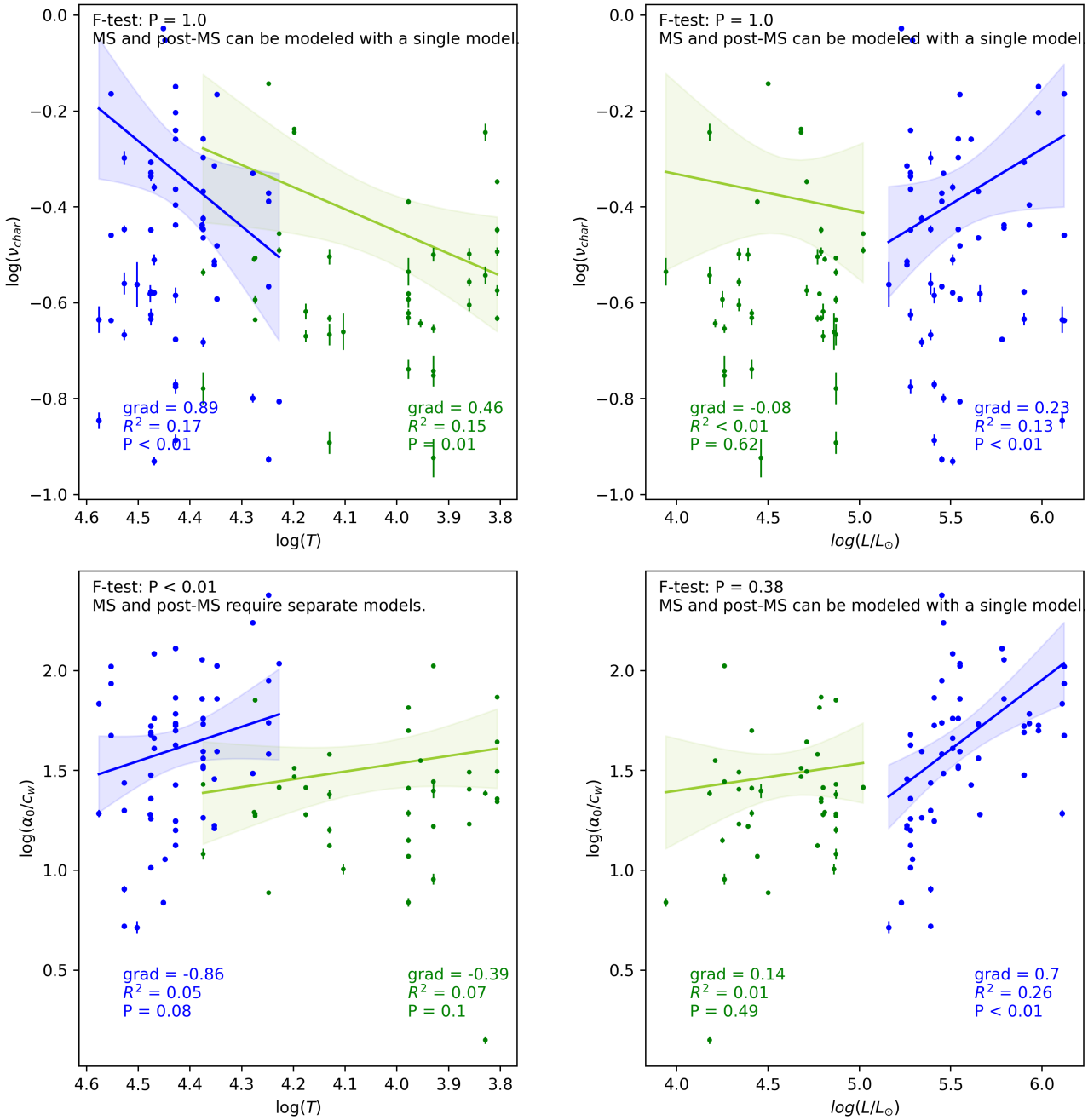

Figure 14. Overview of SLF variability parameters for $T_{\rm eff}$ versus luminosity, which have been done independently for the high mass main sequence (blue) and lower mass post-main sequence (green) subgroups, together with a 95% confidence interval for each linear regression. These two subgroups are also shown as regions in the HR diagram in Fig. 12. The gradient, R^2 and p-values of each linear regression is shown in their respective colours. The top textbox shows results of the F-test for comparing nested linear regression models. The blue filled region indicates a luminosity regime in which both main sequence and post main sequence stars are present, and the systematically higher SLF variability amplitudes are clear for the post-main sequence subgroup of stars.

of this unique sample will open a new window for probing stellar interiors at low metallicities for improving stellar evolution models. Finally, our study serves as a proof-of-concept for the upcoming PLATO mission (Rauer et al. 2025), which will observe the LMC within its 2-yr pointing in the southern hemisphere. With excellent CCD image data provided by PLATO, we will be able to apply our PSF fitting software and extract thousands of variable massive stars for the wider community.

ACKNOWLEDGEMENTS

The TESS data presented in this paper were obtained from the Mikulski Archive for Space Telescopes (MAST) at the Space Telescope Science Institute (STScI), which is operated by the Association of Universities for Research in Astronomy, Inc., under NASA contract NAS5-26555. Support to MAST for these data is provided by the NASA Office of Space Science via grant NAG5-7584 and by other

grants and contracts. Funding for the TESS mission is provided by the NASA Explorer Program.

DMB gratefully acknowledges UK Research and Innovation (UKRI) in the form of a Frontier Research grant under the UK government's ERC Horizon Europe funding guarantee (SYMPHONY; PI Bowman; grant number: EP/Y031059/1), and a Royal Society University Research Fellowship (PI Bowman; grant number: URF\R1\231631). TS acknowledges support from the European Research Council (ERC) under the European Union's Horizon 2020 research and innovation program (grant agreement 101164755/METAL) and from the Israel Science Foundation (ISF) under grant number 0603225041.

DATA AVAILABILITY

The TESS data presented in this paper were obtained from the Mikulski Archive for Space Telescopes (MAST; `https://archive.stsci.edu/missions-and-data/tess`).

This research made use of `astropy` (Astropy Collaboration et al. 2013), `matplotlib` (Hunter 2007), `numpy` (Harris et al. 2020), `Pandas` (McKinney 2010), `Lightkurve` (Lightkurve Collaboration et al. 2018a,b), `TESScut` (Brasseur et al. 2019), `Photutils` (Bradley et al. 2022) and `Period04` (Lenz & Breger 2005).

For the purpose of open access, the authors have applied a CC BY licence to the author accepted manuscript version: `https://arxiv.org/abs/TBD`.

Data products that support the results in this paper are publicly available via the Zenodo repository: `https://zenodo.org/records/TBD`.

REFERENCES

Abbott B. P., et al., 2016, ApJ, 818, L22
Abdul-Masih M., et al., 2016, AJ, 151, 101
Aerts C., 2021, Reviews of Modern Physics, 93, 015001
Aerts C., Rogers T. M., 2015, ApJ, 806, L33
Aerts C., Puls J., Godart M., Dupret M.-A., 2009, A&A, 508, 409
Aerts C., Christensen-Dalsgaard J., Kurtz D. W., 2010, Asteroseismology. Springer, doi:10.1007/978-1-4020-5803-5
Aerts C., Mathis S., Rogers T. M., 2019, ARA&A, 57, 35
Anders E. H., et al., 2023, Nature Astronomy, 7, 1228
Astropy Collaboration et al., 2013, A&A, 558, A33
Bestenlehner J. M., et al., 2025, MNRAS, 540, 3523
Bodensteiner J., et al., 2025, A&A, 698, A38
Boussiala M., 2020, Applied Linear Statistical Models
Bowman D. M., 2020, Frontiers in Astronomy and Space Sciences, 7, 70
Bowman D. M., 2023, Ap&SS, 368, 107
Bowman D. M., Dorn-Wallenstein T. Z., 2022, A&A, 668, A134
Bowman D. M., et al., 2019a, Nature Astronomy, 3, 760
Bowman D. M., et al., 2019b, A&A, 621, A135
Bowman D. M., Burssens S., Simón-Díaz S., Edelmann P. V. F., Rogers T. M., Horst L., Röpke F. K., Aerts C., 2020, A&A, 640, A36
Bowman D. M., et al., 2022, A&A, 658, A96
Bowman D. M., Van Daele P., Michielsen M., Van Reeth T., 2024, A&A, 692, A49
Bradley L., et al., 2022, astropy/photutils: 1.5.0, doi:10.5281/zenodo.6825092, `https://doi.org/10.5281/zenodo.6825092`
Brasseur C. E., Phillip C., Fleming S. W., Mullally S. E., White R. L., 2019, Astrocut: Tools for creating cutouts of TESS images, Astrophysics Source Code Library, record ascl:1905.007 (ascl:1905.007)
Britavskiy N., et al., 2025, arXiv e-prints, p. arXiv:2502.12239
Burssens S., et al., 2020, A&A, 639, A81
Burssens S., et al., 2023, Nature Astronomy, 7, 913
Chiavassa A., et al., 2011, A&A, 528, A120
Crowther P., Bestenlehner J., 2025, arXiv e-prints, p. arXiv:2510.25871
Debnath D., Sundqvist J. O., Moens N., Van der Sijpt C., Verhamme O., Poniatowski L. G., 2024, A&A, 684, A177
Diago P. D., Gutiérrez-Soto J., Fabregat J., Martayan C., 2008, A&A, 480, 179
Dziembowski W. A., Pamyatnykh A. A., 1993, MNRAS, 262, 204
Edelmann P. V. F., Ratnasingam R. P., Pedersen M. G., Bowman D. M., Prat V., Rogers T. M., 2019, ApJ, 876, 4
Feinstein A. D., et al., 2019, PASP, 131, 094502
Gaia Collaboration et al., 2016, A&A, 595, A1
Gaia Collaboration et al., 2021, A&A, 649, A1
Gaia Collaboration et al., 2023, A&A, 674, A1
Garcia S., Van Reeth T., De Ridder J., Tkachenko A., IJspeert L., Aerts C., 2022, A&A, 662, A82
Han T., Brandt T. D., 2023, AJ, 165, 71
Harris C. R., et al., 2020, Nature, 585, 357
Higgins M. E., Bell K. J., 2023, AJ, 165, 141
Hopkins P. F., Kereš D., Oñorbe J., Faucher-Giguère C.-A., Quataert E., Murray N., Bullock J. S., 2014, MNRAS, 445, 581
Howell S. B., 2006, Handbook of CCD Astronomy. Cambridge University Press
Humphreys R. M., Davidson K., 1979, ApJ, 232, 409
Hunter J. D., 2007, Computing in Science & Engineering, 9, 90
Hunter I., et al., 2007, A&A, 466, 277
Jenkins J. M., et al., 2016, in Chiozzi G., Guzman J. C., eds, Society of Photo-Optical Instrumentation Engineers (SPIE) Conference Series Vol. 9913, Software and Cyberinfrastructure for Astronomy IV. p. 99133E, doi:10.1117/12.2233418
Jermyn A. S., Anders E. H., Cantiello M., 2022, ApJ, 926, 221
Johnston C., 2021, A&A, 655, A29
Kalita A. J., Bowman D. M., Abdul-Masih M., Simón-Díaz S., 2025, A&A, 703, A2
Kippenhahn R., Weigert A., Weiss A., 2012, Stellar Structure and Evolution. Springer, Berlin, doi:10.1007/978-3-642-30304-3
Kurtz D. W., Shibahashi H., Murphy S. J., Bedding T. R., Bowman D. M., 2015, MNRAS, 450, 3015
Labadie-Bartz J., Carciofi A. C., Henrique de Amorim T., Rubio A., Luiz Figueiredo A., Ticiani dos Santos P., Thomson-Paressant K., 2022, AJ, 163, 226
Langer N., 2012, ARA&A, 50, 107
Lennon D. J., et al., 2025, arXiv e-prints, p. arXiv:2512.12102
Lenz P., Breger M., 2005, Communications in Asteroseismology, 146, 53
Lightkurve Collaboration et al., 2018a, Lightkurve: Kepler and TESS time series analysis in Python, Astrophysics Source Code Library (ascl:1812.013)
Lightkurve Collaboration et al., 2018b, Lightkurve: Kepler and TESS time series analysis in Python, Astrophysics Source Code Library (ascl:1812.013)
Maeder A., Meynet G., 2000, Annual Review of Astronomy and Astrophysics, 38, 143
Marchant P., Bodensteiner J., 2024, ARA&A, 62, 21
McKinney W., 2010, in van der Walt S., Millman J., eds, Proceedings of the 9th Python in Science Conference. pp 51 – 56
Miglio A., Montalbán J., Dupret M.-A., 2007, MNRAS, 375, L21
Nardiello D., et al., 2019, MNRAS, 490, 3806
Pápics P. I., et al., 2017, A&A, 598, A74
Patrick L. R., et al., 2025, A&A, 698, A39
Pauli D., et al., 2023, A&A, 673, A40
Prša A., et al., 2022, ApJS, 258, 16
Rauer H., et al., 2025, Experimental Astronomy, 59, 26
Ricker G., 2021a, in 43rd COSPAR Scientific Assembly. Held 28 January - 4 February. p. 499
Ricker G., 2021b, in 43rd COSPAR Scientific Assembly. Held 28 January - 4 February. p. 499
Ricker G. R., et al., 2015, Journal of Astronomical Telescopes, Instruments, and Systems, 1, 014003

Rogers T. M., McElwaine J. N., 2017, ApJ, 848, L1
Rogers T. M., Lin D. N. C., McElwaine J. N., Lau H. H. B., 2013, ApJ, 772, 21
Salmon S., Montalbán J., Morel T., Miglio A., Dupret M. A., Noels A., 2012, MNRAS, 422, 3460
Sana H., et al., 2012, Science, 337, 444
Sana H., et al., 2025, Nature Astronomy, 9, 1337
Schootemeijer A., Langer N., Grin N. J., Wang C., 2019, A&A, 625, A132
Schultz W. C., Bildsten L., Jiang Y.-F., 2022, ApJ, 924, L11
Schwarz G., 1978, The Annals of statistics, 6, 461
Scott L. J. A., Bowman D. M., 2026, MNRAS, 545, staf2174
Shenar T., et al., 2024, A&A, 690, A289
Soszyński I., et al., 2023, Acta Astron., 72, 245
Stankov A., Handler G., 2005, ApJS, 158, 193
Thompson W., Herwig F., Woodward P. R., Mao H., Denissenkov P., Bowman D. M., Blouin S., 2024, MNRAS, 531, 1316
Udalski A., Szymański M. K., Szymański G., 2015, Acta Astron., 65, 1
Van Daele P., 2023, Master's thesis, KU Leuven
Varghese A., Ratnasingam R. P., Vanon R., Edelmann P. V. F., Rogers T. M., 2023, ApJ, 942, 53
Varghese A., Ratnasingam R. P., Ramírez-Galeano L., Mathis S., Rogers T. M., 2025, ApJ, 992, L5

APPENDIX A: VARIABILITY CLASSIFICATION FOR ALL PSF OBSERVED BLOEM STARS

Table A1: Overview of stars with PSF light curves and their variability type.

GAIA DR3 ID	BLOeM ID	Tmag	Spectral Type	TESS PSF light curve Variability
4685835884339219456	BLOeM 3-037	12.3	B3 Ia	SLF (long period)
4685854571724688768	BLOeM 3-012	12.9	sgB[e]	SLF (long period)
4685943121123943680	BLOeM 3-043	11.0	A2 Iab	SLF
4685943254211136000	BLOeM 3-061	12.0	B3 Ib	noisy / constant
4685945010910000640	BLOeM 3-106	13.6	B5 Ib	contaminated (RR Lyr? Cepheid?)
4685947553531340800	BLOeM 3-042	11.2	O6 I(f)	EV or RotMod (nice example if matches spectra period)
4685959373284393728	BLOeM 2-072	13.9	A2 II/Ib	contaminated (RR Lyr? Cepheid?)
4685972636146149504	BLOeM 7-064	12.3	B0 Ia	SLF
4685976621875402368	BLOeM 7-075	13.0	B8 Ib	
4685983420730442624	BLOeM 2-113	12.4	B2.5 Ia	SLF (long period) (nice example)
4685987857514223744	BLOeM 7-004	13.7	A0 Iab	missing figure?
4686408111398825728	BLOeM 6-015	12.6	F2:	noisy / constant
4686410550940229888	BLOeM 6-095	14.0	A0 Ib	
4686410688379157888	BLOeM 6-108	13.2	A0 Iab	
4686410997616777984	BLOeM 6-105	14.3	O6 V:n	
4686413230999834496	BLOeM 6-067	14.3	O9.7 III	
4686413437158238208	BLOeM 6-080	12.1	B0 Ia	SLF (nice example!)
4686413540237697408	BLOeM 6-072	14.4	B3 II	missing figure?
4686413810818254464	BLOeM 6-093	14.2	O8.5 V	
4686414467950355072	BLOeM 6-076	13.0	B0 Ib	
4686417148009897344	BLOeM 6-116	13.4	A7 Iab	
4687157286836619520	BLOeM 6-007	15.2	B5 II	contaminated (RR Lyr? Cepheid?)
4687158592506675328	BLOeM 6-006	12.3	F2:	noisy / constant
4687159868124113152	BLOeM 6-008	10.0	A2 Ia	noisy / constant
4687161895348646400	BLOeM 6-005	13.8	O9.7 II-Ib(n)	
4687161929708394752	BLOeM 6-002	12.8	A2 Ib	
4687162582543422080	BLOeM 6-001	14.0	B0.5 III: e	
4687164055705068288	BLOeM 6-024	11.5	A5 Iab	missing figure?
4687165125163949952	BLOeM 6-017	13.4	B1 Ib	
4687165709279578368	BLOeM 6-052	12.8	A2 II/Ib	noisy / constant
4687167152388524032	BLOeM 6-084	14.2	O9.7 I:(n)	SLF (noisy)
4687426087389568768	BLOeM 7-108	14.0	B2.5 Ia	SLF (noisy)
4687437254305162880	BLOeM 5-071	13.5	O8.5: Ib	SLF (nice example!)
4687437426103845376	BLOeM 5-091	13.1	B8 Ib	
4687478138084449536	BLOeM 7-111	12.6	B0 Ia	missing figure?
4687479173187523584	BLOeM 7-091	11.3	A5 Iab	
4687485387976612736	BLOeM 5-067	12.4	A0 Iab	noisy / constant
4687485491055825536	BLOeM 5-077	12.4	B2.5 Ia	SLF
4687487213367243392	BLOeM 5-029	12.9	A7 Ib	puls (nice example!)
4687487900566335744	BLOeM 5-014	13.0	A0 Ib	
4687499720314663296	BLOeM 5-012	13.5	A2 II/Ib	
4687501953697501568	BLOeM 5-050	14.0	O9.7 V:	EV or RotMod (nice example if matches spectra period)
4687503946562429184	BLOeM 1-085	13.1	A7 Ib/ab	
4687504182822540416	BLOeM 5-005	13.4	F2:	LBV or AGB (F supergiant)
4687505389671548672	BLOeM 1-065	12.9	A7 Ib	
4687505801988031232	BLOeM 1-106	13.6	B1.5 e	SLF (eclipses?)
4687507245097014144	BLOeM 1-112	11.2	B9 Ia	noisy / constant
4687507584364583040	BLOeM 1-111	11.4	B3 Ia	
4687508413319210368	BLOeM 5-102	13.4	F0:	
4687509749039520768	BLOeM 5-105	13.4	B0.7 II	
4687512948804514176	BLOeM 5-104	13.8	B2.5 Ia	SLF (noisy)
4687513910877142528	BLOeM 5-090	14.1	O9.5 III	contaminated (RR Lyr? Cepheid?)
4688962517474878720	BLOeM 2-080	13.5	A2 II/Ib	constant
4688966292708802304	BLOeM 2-054	12.1	A0 Ia	noisy / constant
4688967289176997504	BLOeM 2-092	12.3	B8 Iab	noisy / constant

Continued on next page

Table A2 (continued)

GAIA DR3	BLOeM ID	Tmag	Spectral Type	TESS PSF light curve Variability
4688967362197739392	BLOeM 2-093	10.8	B8 Ia	long period (nice example to help spectra period)
4688967568356557440	BLOeM 2-065	10.7	F5:	constant
4688978838366817280	BLOeM 2-007	12.7	O9.5 II-I	SLF (nice example!)
4688980414561766016	BLOeM 2-068	13.0	B9 Iab	
4688986534938381184	BLOeM 2-116	12.9	sgB[e]	missing figure?
4689002851458876800	BLOeM 4-006	11.4	F2:	noisy / constant
4689003027613801216	BLOeM 4-020	12.9	B1 Iab-Ib	SLF (nice example!)
4689018661298288000	BLOeM 4-001	13.3	A1 Ib	
4689033539046230400	BLOeM 8-010	11.4	A0 Ia	long period (nice example to help spectra period)
4689037181200454656	BLOeM 8-006	13.8	B2.5 II-Ib	EV or RotMod (or SLF?)
4689054670286883968	BLOeM 8-001	13.0	B8 Ib	constant
4689054945164735616	BLOeM 8-008	12.8	B1 Iab	SLF
4689057346006300544	BLOeM 8-072	11.9	F2:	contaminated (RR Lyr? Cepheid?)
4689058892200836096	BLOeM 8-116	13.0	A2 Ib	contaminated (RR Lyr? Cepheid?)
4689058999614762368	BLOeM 8-097	13.5	F0:	contaminated (EB?)
4689061920192649984	BLOeM 8-082	13.1	B9 Iab	constant
4689062298150064640	BLOeM 8-022	13.8	B0.5 II	SLF and RotMod
4689074598938187776	BLOeM 8-053	14.3	O9 III	contaminated (RR Lyr? Cepheid?)
4690500047016009728	BLOeM 4-103	12.6	A5 Ib	constant
4690500184455105536	BLOeM 4-072	12.5	B9 Ia	constant
4690502280398443776	BLOeM 1-053	13.9	B1 Ib	noisy / constant
4690502280398446720	BLOeM 1-051	10.8	A0 Ia	long period?
4690503306873686912	BLOeM 1-039	12.8	A2 II/Ib	noisy / constant
4690503826587160832	BLOeM 4-078	12.3	B1 Ia	SLF (nice example!)
4690506712804881792	BLOeM 1-011	14.3	B1.5 II	EV or RotMod
4690506914646214912	BLOeM 1-016	12.1	A2 Ib	constant
4690507670561677696	BLOeM 1-031	12.6	A0 Iab	missing figure?
4690507881037706112	BLOeM 1-062	13.1	B8 Iab	contaminated (RR Lyr? Cepheid?)
4690508632639753984	BLOeM 1-095	12.9	B1 Ia	SLF (noisy)
4690516677131714432	BLOeM 4-058	11.2	O7 Iaf$^+$	SLF (nice example!)
4690519769509887488	BLOeM 1-028	12.3	B8 Iab/Ia	noisy / constant
4690520387983090432	BLOeM 1-009	12.6	B1 Ia	SLF (nice example!)
4690521762372716160	BLOeM 4-079	13.3	A0 Ib	
4690522002890799488	BLOeM 4-084	12.8	A0 Iab	
4690522273449262592	BLOeM 4-055	12.5	sgB[e]	SLF (long period)
4690525438865707904	BLOeM 1-040	13.7	O9.7 III:n e	puls (nice example!)

This paper has been typeset from a TEX/LATEX file prepared by the author.